Fast Evaluation of RF Power Spectrum of Photodetectors With Windowing Functions

Ergun Simsek, *Senior Member, IEEE*, Ishraq Md Anjum, *Graduate Student Member, IEEE*,
Thomas F. Carruthers, *Member, IEEE*, Curtis R. Menyuk, *Life Fellow, IEEE*,
Joe C. Campbell, *Life Fellow, IEEE*, David A. Tulchinsky, *Member, IEEE*, and Keith J. Williams

Abstract— **Time window functions are used as broadband excitations to obtain the output power spectrum of photodetectors. Numerical results show a good agreement with experimental results. The proposed method yields a two-orders-of-magnitude reduction in computing time and memory compared to traditional monochromatic calculations. This large reduction makes it possible to design high-performance photodetectors with numerical optimization on desktop computers. We use this approach to design a device whose 3-dB bandwidth is four times larger than the initial design.**

Index Terms— **Drift-diffusion equations, photodetectors, photodiodes.**

I. Introduction

SEMICONDUCTOR photodetectors, which convert incident optical signals into electrical currents, are widely used in optical communication and other opto-electronic and RF-photonic applications that require large bandwidth, high efficiency, and low dark current [1], [2], [3], [4], [5], [6], [7], [8], [9], [10]. The compression currents of photodetectors are currently a critical bottleneck in the effort to increase the compression dynamic range of analog optical links [5]. Different designs have been proposed to overcome this challenge [1], [2], [6], [7], [8], [9], [10]. Uni-traveling carrier (UTC) photodetectors have been developed that achieve a high bandwidth by minimizing unwanted space charge that limits the output RF power of photodetectors [6]. modified UTC (MUTC) photodetectors further improve upon the UTCs and can support higher output currents [2], [7], [8], [9]. Alternative designs have been proposed [11], [12] that are expected to improve the device performance, but determining

the optimal design that meets all the design requirements is a nontrivial task due to the design trade-offs [1], [2], [3], [4], e.g., smaller photodetectors have a larger bandwidth but generate a weaker output current. In order to characterize a photodetector's performance, it is necessary to find the photodetector's RF output power spectrum either experimentally or numerically. Obtaining numerical results quickly can help to reduce computational costs and save time.

One can calculate the output power of a photodetector by solving the drift-diffusion equations [4], [13] using a single-frequency (monochromatic) modulation of the input optical power. By repeating the same procedure over the entire frequency range of interest, one can obtain the RF output power spectrum with high accuracy. The use of parallel computing resources can reduce the computation time since the response to each frequency modulation is calculated independently. On the other hand, one can obtain the entire spectrum in one run by using broadband modulation. For example in [14], we use a sinc function as a broadband modulation, which carries the signature of all the frequencies from dc to a desired limit almost at the same strength. However, a sinc–function has a long oscillatory tail that only slowly decays, so a simulation that uses it requires a long simulation time, which has to be tens or even one hundred times the period that corresponds to the highest frequency of interest in order to obtain high accuracy. These long integration times imply that much of the advantage that is gained by just computing the response to a single modulation is lost. However, some applications do not require very high accuracy. For example, when the goal is trying to design a high bandwidth photodetector via numerical optimization, it is desirable to rapidly obtain a rough determination of the decrease in performance over the bandwidth of the device, which in the case of a MUTC photodetector might be between 1 and 100 GHz.

We can in principle avoid the necessity of determining the response individually at each frequency by using a broadband modulation function that has a more rapid falloff in time. However, this more rapid falloff in time leads to a falloff in the input optical frequency at high frequencies that is not present with the sinc function. This falloff can decrease the accuracy of the result. Due to the uncertainty principle, the rate of falloff of a given modulation, which is characterized by the 3-dB bandwidth, is proportional to the duration of the

This article has been accepted for inclusion in a future issue of this journal. Content is final as presented, with the exception of pagination.
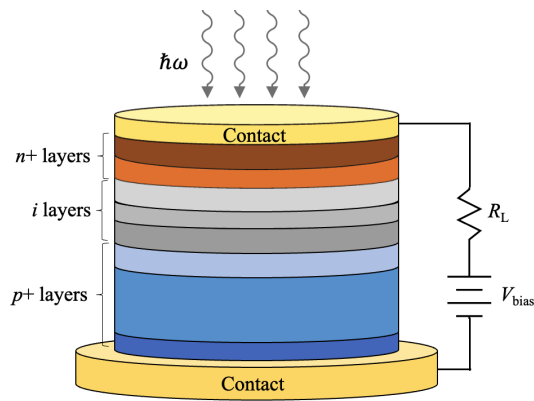
2

IEEE TRANSACTIONS ON ELECTRON DEVICES

Fig. 1. Illustration of a reverse-biased photodetector illuminated from its *n*-side. Thin yellow layers represent the contacts.
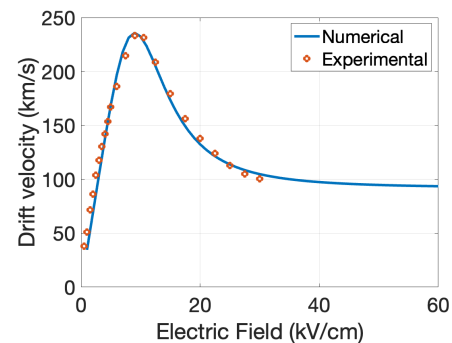

Fig. 2. Electron drift velocity of InP as a function of local electric field intensity. The blue curve is obtained with the (3a) using the parameters listed in Table I. The red circles are the experimental results [17].

modulation. Hence, there is a tradeoff between the duration of the modulation and accuracy. This observation suggests a two-stage design process. In the first stage, we use lower-accuracy results for an initial optimization. In the second stage, we validate these results using more accurate results that we can obtain using monochromatic excitations.

Both in signal processing [26], [27] and time domain modeling of electromagnetic [28] and geophysical [29] systems, window functions are commonly used to evaluate the broadband response of a system. The advantage of using these special window functions is that they are smooth and—unlike the sinc function—they diminish very fast in the time domain. Hence, compared to the other two options (multiple monochromatic simulations or a single simulation with a sinc modulation), the use of these window functions to modulate the input optical power is expected to require less computational time for the simulation at the expense of reduced accuracy, especially at the higher frequencies. In this work, we first quantify this error and compare the numerical results with experiments that were carried out using a recently fabricated MUTC photodetector that we will describe shortly. Then we use this fast method in combination with the particle swarm optimization (PSO) [30], [31], [32] algorithm to design a MUTC photodetector with a higher bandwidth. Finally, we compare the RF spectrum of the optimized device that we obtained using broadband modulation to the RF spectrum of the same device using monochromatic modulation. The results are in excellent agreement, thereby validating the overall approach's efficiency and accuracy.

II. DRIFT-DIFFUSION EQUATIONS

Fig. 1 illustrates a reverse-biased photodetector illuminated from the top.

Our formulation starts with the electron and hole continuity equations and the Poisson equation

$$\frac{\partial(p - n_A^-)}{\partial t} = -\frac{1}{q}\nabla \cdot \mathbf{J}_p + G_{ii} + G_{opt} - R(n, p) \quad (1a)$$

$$\frac{\partial(n - N_D^+)}{\partial t} = +\frac{1}{q}\nabla \cdot \mathbf{J}_n + G_{ii} + G_{opt} - R(n, p) \quad (1b)$$

$$\nabla \cdot \mathbf{E} = \frac{q}{\epsilon}(n - p + N_A^- - N_D^+) \quad (1c)$$

where n is the electron density, p is the hole density, t is time, q is the unit of charge, $\mathbf{J}_n$ is the electron current density, $\mathbf{J}_p$ is the hole current density, R is the recombination rate, G_{ii} and G_{opt} are impact ionization and optical generation rates, $\mathbf{E}$ is the electric field at any point in the device, ϵ is the electrical permittivity, N_A^- is the ionized acceptor concentration, and N_D^+ is the ionized donor concentration. The electron and hole current densities are governed by the equations

$$\mathbf{J}_p = qp\mathbf{v}_p(\mathbf{E}) - qD_p\nabla p \quad (2a)$$

$$\mathbf{J}_n = qn\mathbf{v}_n(\mathbf{E}) + qD_n\nabla n \quad (2b)$$

where $\mathbf{v}_n(\mathbf{E})$ and $\mathbf{v}_p(\mathbf{E})$ are the electric-field-dependent electron and hole drift velocities, D_n and D_p are the electron and hole diffusion coefficients, respectively. We use the following empirical expressions for $\mathbf{v}_n(\mathbf{E})$ [15] and $\mathbf{v}_p(\mathbf{E})$ [16] to fit the measured results:

$$\mathbf{v}_n(\mathbf{E}) = \frac{\mathbf{E}(\mu_n + v_{n,sat}\beta|\mathbf{E}|)}{1 + \beta|\mathbf{E}|^2} \quad (3a)$$

$$\mathbf{v}_p(\mathbf{E}) = \frac{\mu_p v_{p,sat}\mathbf{E}}{(v_{p,sat}^\gamma + \mu_p^\gamma|\mathbf{E}|^\gamma)^{1/\gamma}} \quad (3b)$$

where μ_n is the electron low-field mobility, $v_{n,sat}$ is the saturated electron velocity, β is a fitting parameter, μ_p is the hole low-field mobility, γ is an empirical fitting parameter that depends on temperature, and $v_{p,sat}$ is the saturated hole velocity. See Fig. 2 as an example.

To take into account the dependence of electron and hole low field mobilities, μ_n and μ_p, on the doping density, we define

$$\mu_{n,p} = \frac{\mu_{n_0, p_0}}{1 + \left(\frac{N_D + N_A}{N_{ref}}\right)^\eta} \quad (4)$$

where μ_{n_0} and μ_{p_0} are electron and hole mobilities at low doping concentrations, respectively, while N_{ref} and η are empirical parameters. The electric field-dependent electron and hole diffusion coefficients are calculated with [18]

$$D_n(\mathbf{E}) = \frac{k_B T \mu_n/q}{\left[1 - 2(|\mathbf{E}|/E_P)^2 + \frac{4}{3}(|\mathbf{E}|/E_P)^3\right]^{1/4}} \quad (5a)$$

$$D_p(\mathbf{E}) = \frac{k_B T}{q}\frac{\mathbf{v}_p(\mathbf{E})}{\mathbf{E}} \quad (5b)$$

where E_p is the electric field at which the diffusion constant peaks. The recombination rate in (1a) includes three terms: Auger recombination, $R_{\text{Auger}} = (C_n n + C_p p)\varphi$, radiative recombination, $R_{\text{rad}} = B_r \varphi$, and the Shockley-Read-Hall effect (R_{SRH}), which is defined as follows [19]:

$$R_{\text{SRH}} = \frac{\varphi}{\tau_p(n + n_i) + \tau_n(p + n_i)} \qquad (6)$$

where $\varphi = np - n_i^2$, τ_n and τ_p are the electron and hole lifetimes, n_i is intrinsic carrier density, respectively, C_n and C_p are the Auger recombination rate for electrons and holes, and B_r is the radiative recombination coefficient.

The optical generation rate in (1a) is $G_{\text{opt}}(x, t) = G_c(t)e^{-\alpha(L-x)}$, where α is the absorption coefficient, x is the distance across the device, L is the device length, and $G_c(t)$ is the generation rate coefficient as a function of time, which is given by $G_c(t) = \alpha P_{\text{opt}}(t)/A W_{\text{photon}}$, where $P_{\text{opt}}(t)$ is the optical power as a function of time, A is the area of the light spot, and W_{photon} is the photon energy [20]. Note that the generation rate in the absorption layer depends on the location of the device as well as the material. The total output current (J_t) is the sum of the hole (J_h), electron (J_e), and displacement currents $(J_d = \epsilon \partial E / \partial t)$.

Our model accounts for the incomplete ionization of doping impurities such as boron, aluminum, and nitrogen, using the following expressions [20], [21]:

$$N_D^+ = N_D\left[1 + g_D \exp\left(\frac{E_{Fn} - E_D}{k_B T}\right)\right]^{-1} \qquad (7a)$$

$$N_A^- = N_A\left[1 + g_A \exp\left(\frac{E_A - E_{Fp}}{k_B T}\right)\right]^{-1} \qquad (7b)$$

where N_D and N_A are the donor and acceptor impurity concentrations, g_D and g_A are the respective ground-state degeneracy of donor and accept impurity levels [3], [22], E_A and E_D are the acceptor and donor energy levels, E_C and E_V are the low conduction band and the high valence band energy levels, E_{Fn} and E_{Fp} are the quasi-Fermi energy levels for the electrons and holes, and T is the temperature. The electron and hole generation rate due to impact ionization G_{ii} can be described as follows [23]:

$$G_{\text{ii}} = \alpha_n \frac{|\mathbf{J}_n|}{q} + \alpha_p \frac{|\mathbf{J}_p|}{q} \qquad (8)$$

where α_n and α_p are the impact ionization coefficients of the electrons and holes, respectively. We calculate their values using the formulae [23], [24]

$$\alpha_n = A_n \cdot e^{-B_n/|\mathbf{E}|} \text{ and } \alpha_p = A_p \cdot e^{-B_p/|\mathbf{E}|} \qquad (9)$$

where A_n, B_n, A_p, and B_p are experimentally-determined parameters [24], [25]. The parameters for InGaAs and InP—the two semiconductor materials that are used in our calculations—are listed in Table I.

III. Broadband Modulation

We write the input optical power as $P_{\text{in}}(t) = P_0 \times \{1 + m \times F_{\text{mod}}(t)\}$, where P_0 is the strength of the excitation, m is the modulation depth, t is time, and $F_{\text{mod}}(t)$ is the modulation function. We can define a monochromatic or

TABLE I
MATERIAL PARAMETERS AT 300 K THAT ARE USED IN OUR CALCULATIONS. m_0 IS THE ELECTRON MASS

Parameter	InP	In$_{0.53}$Ga$_{0.47}$As
E_g (eV)	1.28	0.74
χ (eV)	4.38	4.51
ϵ_r (eV)	12.4	13.7
$\tau_{n,p}$ in i-region (ns)	10	10
$\tau_{n,p}$ in doped region (ps)	100	100
A_n (cm^{-1})	1.12×10^7	6.64×10^7
B_n (V/cm)	6.2×10^6	4×10^6
A_p (cm^{-1})	4.79×10^6	9.34×10^7
B_p (V/cm)	2.55×10^6	2.26×10^6
$\mu_{n,0}$ (cm^2/V sec)	5300	13000
$\mu_{p,0}$ (cm^2/V sec)	200	630
N_C (cm^{-3})	5.71×10^{17}	2×10^{17}
N_V (cm^{-3})	1.14×10^{19}	5.48×10^{18}
$N_{n,\text{ref}}$ (cm^{-3})	10^{17}	10^{17}
$N_{p,\text{ref}}$ (cm^{-3})	6×10^{17}	10^{18}
η_n	0.34	0.5
η_p	0.64	0.45
β (cm^2/V^2)	8×10^{-8}	4×10^{-8}
$v_{n,\text{sat}}$ (cm/sec)	6.7×10^6	7.67×10^8
$v_{p,\text{sat}}$ (cm/sec)	5×10^6	6.39×10^6
m_n^*/m_0	0.08	0.041
m_p^*/m_0	0.64	0.59
C_n (cm^6/s)	1.8×10^{-31}	10^{-31}
C_p (cm^6/s)	1.2×10^{-31}	10^{-31}
B_r (cm^3/s)	10^{-10}	10^{-11}
γ	1	1

broadband modulation using various function types. Fig. 3(a) shows examples of cosine, sinc, and Blackman-Harris window functions that we will refer to respectively as monochromatic, broadband-sinc, and broadband-window. The explicit form of these functions is given by the following equation:

$$F_{\text{mod}}(t) = \cos(2\pi f_i t) \qquad (10a)$$

$$F_{\text{mod}}(t) = \text{sinc}[2 \times f_{\text{mod}}^{\text{max}} \times (t - t_c)] \qquad (10b)$$

$$F_{\text{mod}}(t) = \frac{1}{L}\sum_{n=0}^{N} a_n \cos\left(\frac{2\pi n(t - t_c)}{L}\right) \text{ for } |t - t_c| \leq \frac{L}{2} \qquad (10c)$$

respectively, where f_i is an individual frequency value of interest, $f_{\text{mod}}^{\text{max}}$ is the highest frequency of interest, T_{max} is the largest t value, t_c is the pulse central time, and $L = 1/f_{\text{mod}}^{\text{max}}$. The coefficients $\{a_n\}_0^N$ are real constants that determine the characteristics of the windowing function. The rules for selecting the values of a_n may be found in [26] and [27]. In this work, three of the most commonly used windowing functions are implemented: the minimum four-term Blackman-Harris, the four-term continuous third derivative Nuttall, and the five-term flat-top with the values of a_n listed in Table II.

Fig. 3(b) shows frequency content of these three functions. As expected, the monochromatic modulation shows a peak at the frequency f_i, and the sinc function has an almost constant strength from $f = 0$ GHz to $f_{\text{mod}}^{\text{max}}$, and the window function includes all frequencies up to and beyond $f_{\text{mod}}^{\text{max}}$, but with a magnitude that decreases with increasing frequency.

For the monochromatic modulation, the output power is simply

$$I_{\text{rms}}^2(t) \times R_{\text{load}} \qquad (11)$$

4

IEEE TRANSACTIONS ON ELECTRON DEVICES

This article has been accepted for inclusion in a future issue of this journal. Content is final as presented, with the exception of pagination.

TABLE II

COEFFICIENTS IN THE BROADBAND WINDOW FUNCTION FOR THE MINIMUM FOUR-TERM BLACKMAN-HARRIS WINDOW, CONTINUOUS THIRD DERIVATIVE NUTTALL WINDOW, AND FLAT-TOP WINDOW. WE NOTE THAT DIFFERENT REFERENCES PROVIDE SLIGHTLY DIFFERENT COEFFICIENTS, E.G., [26], [27]. AS LONG AS WE NORMALIZE THE PULSE IN THE TIME DOMAIN WITH ITS MAXIMUM VALUE SO THAT $\max[F_{\mathrm{MOD}}(t)] = 1$ AND WE NORMALIZE THE POWER SPECTRUM SO THAT $P_{\mathrm{OUT}}(f = 0) = 1$, THESE DIFFERENCES DO NOT SIGNIFICANTLY CHANGE THE FINAL RESULTS

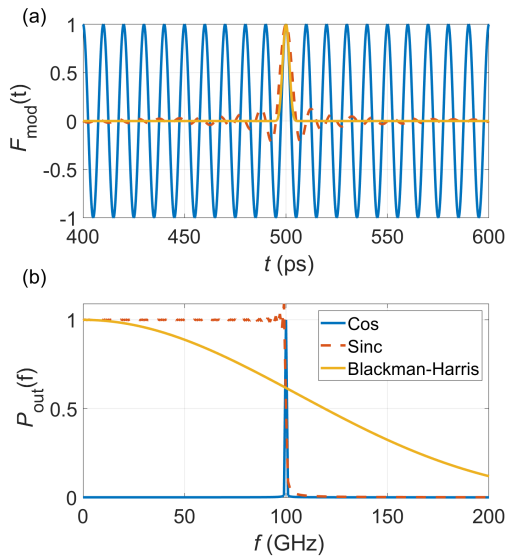| Type	a_0	a_1	a_2	a_3	a_4
Blackman-Harris	0.3532	0.488	0.145	0.01	–
Nuttall	0.3389	0.4819	0.161	0.018	–
Flat-Top	0.2155	0.4166	0.277	0.0836	0.0069

Fig. 3. Three different excitations: $\cos(2\pi f_i t)$, $\mathrm{sinc}[2f_{\mathrm{mod}}^{\max}(t - t_c)]$, and a Blackman-Harris pulse for $T_{\max} = 1$ ns; $\Delta t = 0.1$ ps; $t_c = T_{\max}/2$, $f_{\mathrm{mod}}^{\max} = f_i = 100$ GHz, in (a) time-domain and (b) frequency-domain.

where R_{load} is the load resistance. For the broadband-sinc modulation, the fast Fourier transform (FFT) of the output current is first normalized

$$Y = |\mathrm{FFT}\{I_{\mathrm{rms}}(t)\}| \times n_{\mathrm{periods}}/L \qquad (12)$$

then squared, and then multiplied by $2R_{\mathrm{load}}$, so that

$$P_{\mathrm{out}}(f_i) = 2 \times R_{\mathrm{load}} \times Y^2 \qquad (13)$$

which then yields the entire power spectrum for $0 < f_{\mathrm{spectrum}} \leq f_{\mathrm{mod}}^{\max}$, where

$$L = T/\Delta t, \qquad (14a)$$
$$t = 0 : \Delta t : T, \qquad (14b)$$
$$f_{\mathrm{spectrum}} = f_s \times (0 : L/2)/L/2, \qquad (14c)$$
$$f_s = 1/\Delta t, \qquad (14d)$$
$$n_{\mathrm{periods}} = T \times f_{\mathrm{mod}}^{\max}. \qquad (14e)$$

For the broadband-window modulation, the different frequencies are not represented at the same strength, and we must normalize the spectrum of $I_{\mathrm{rms}}^2(t) \times R_{\mathrm{load}}$ with respect to the

TABLE III

FIRST THREE COLUMNS LIST THE SEMICONDUCTOR TYPES, THICKNESSES (t_i), AND DOPING LEVELS (d_i) FOR THE 15 LAYERS OF THE ORIGINAL MUTC PHOTODETECTOR, I.E., $i = 1, 2, \ldots, 15$. THE LAST TWO COLUMNS LIST THICKNESSES AND DOPING LEVELS FOR THE DESIGN OBTAINED WITH THE OPTIMIZATION THAT ASSUMES SAME MATERIAL AND DOPING TYPES

Material	Original Design t_i (nm)	Original Design d_i (cm^{-3})	Optimized Design t_i (nm)	Optimized Design d_i (cm^{-3})
InGaAs, $p+$	50	2×10^{19}	25	1.0×10^{19}
InP, $p+$	100	2×10^{18}	100	1.25×10^{18}
InGaAsP, Q1.1, $p+$	15	5×10^{18}	50	6.72×10^{18}
InGaAsP, Q1.4, $p+$	15	5×10^{18}	10	2.15×10^{18}
InGaAs, $p+$	120	5×10^{18}	115	1.0×10^{19}
InGaAs, $p+$	180	1.3×10^{18}	50	3.73×10^{18}
InGaAs, $p+$	180	4×10^{17}	255	1.0×10^{17}
InGaAs, $n-$	160	1×10^{16}	284	1.0×10^{15}
InGaAsP, Q1.4, $n-$	15	1×10^{16}	38	1.0×10^{15}
InGaAsP, Q1.1, $n-$	15	1×10^{16}	10	1.22×10^{16}
InP, $n-$	50	1.9×10^{17}	22	2.56×10^{16}
InP, $n-$	300	1.5×10^{16}	240	1.83×10^{16}
InP, $n-$	440	1.2×10^{16}	455	7.27×10^{15}
InP, $n+$	100	1×10^{18}	146	8.79×10^{18}
InP, $n+$	900	1×10^{19}	943	1.0×10^{19}

square of the absolute value of the FFT of $F_{\mathrm{mod}}(t)$, so that

$$P_{\mathrm{out}}(f_i) = \frac{|\mathrm{FFT\ of}\ I_{\mathrm{rms}}^2(t)\ \times R_{\mathrm{load}}\ \mathrm{at}\ f_i|}{|\mathrm{FFT\ of}\ \mathrm{F_{mod}}(t)\ \mathrm{at}\ f_i|^2}. \qquad (15)$$

To verify the efficiency and determine the accuracy of the method, we study a MUTC photodetector next, both experimentally and numerically. We then demonstrate the usefulness of this approach by using it to optimize the device design in order to significantly increase its bandwidth.

IV. VALIDATION AND OPTIMIZATION

Our MUTC photodetector has 15 layers with different semiconductor materials and varying thicknesses and doping levels as listed in the first three columns of Table III. The photodetector is reverse-biased ($V_{\mathrm{bias}} = -9$ V) and is illuminated by a continuous wave laser operation at 1550 nm that is modulated by an input RF signal. The diameters of the incident beam and photodetector are 40 and 28 μm, respectively. The load resistance is 50 Ω. More details of our simulation model may be found in [4].

Fig. 4 compares experimentally-measured RF output spectrum with numerical results that we obtained using a broadband-sinc function and the three broadband-window functions that we defined in (10b) and (10c) that is implemented with the coefficients given in Table II. The accuracy of the broadband-sinc function's implementation depends on our choice of $T_{\max}$; a longer $T_{\max}$ yields a more accurate solution. Here, we use 20 000 time-steps for the broadband-sinc implementation. Time-window implementations do not have such a dependency. For this comparison, we choose 2000 time steps so that the implementation requires 10% of

This article has been accepted for inclusion in a future issue of this journal. Content is final as presented, with the exception of pagination.

SIMSEK et al.: FAST EVALUATION OF RF POWER SPECTRUM OF PHOTODETECTORS WITH WINDOWING FUNCTIONS 5
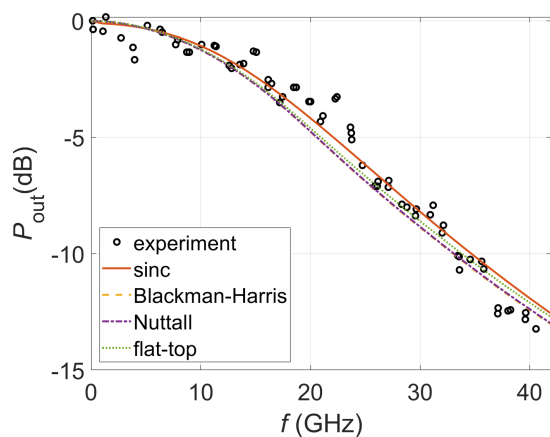

Fig. 4. RF output power spectrum of the original design that is detailed in Table III. Black circles depict the experimental results while red continuous, yellow dashed, magenta dashed-dotted, and green dotted curves show the numerical results for the broadband cases obtained with a sinc, Blackman-Harris, Nuttall, and flat-top window, respectively.

TABLE IV
AVERAGE ERROR (ϵ_{BH}, ϵ_{Nu}, AND ϵ_{FT}) VERSUS Δt FOR
BLACKMAN-HARRIS, NUTTALL, AND FLAT-TOP
WINDOWING FUNCTIONS

Δt (ps)	L	ϵ_{BH} (%)	ϵ_{Nu} (%)	ϵ_{FT} (%)
1	100	1.5323	1.5638	1.811
0.2	500	0.2725	0.234	0.3182
0.1	1000	0.1184	0.0789	0.25341
0.05	2000	0.03974	0.01079	0.12835

the computation time as is the case for the broadband-sinc implementation.

As expected in all cases, the numerical results show excellent agreement with experiments at low frequencies. The differences become visible as we reach the high end of the spectrum. In order to determine how many time steps would be necessary to get a rough estimate of the RF spectrum of a photodiode, we run three additional sets of numerical calculations, where in each run, we increase Δt by decreasing L, the number of time steps, from 2000 to 100. We take the simulation results obtained with the broadband-sinc modulation function and 20 000 time steps as the ground truth. As listed in Table IV, we see that the average error increases steadily but even for the worst case, where we use only 100 time steps, the average error is still less than 2%.

Using 100 time steps instead of 20 000 leads to a reduction in the computation time and memory usage by almost a factor of 200. While the broadband-window modulation functions yield errors on the order of 2% at high frequencies, these errors are not large enough to significantly affect device optimization. In order to verify this claim, we use the proposed method as the forward solver in a particle-swarm optimization (PSO) implementation in which the material and doping types are fixed, the doping density and thickness of each layer are the variables to be optimized, and the cost function is simply the sum of the absolute value of the entire RF output power spectrum. For the PSO algorithm, we use a swarm size of 300. We ran the optimization algorithm on a desktop computer and
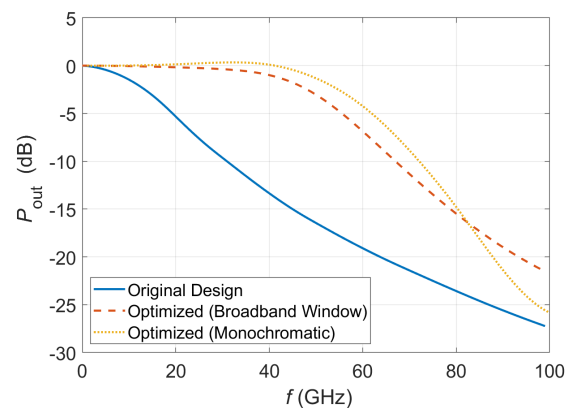

Fig. 5. RF output power spectrum of the original design (blue curve) and optimized design. The red dashed lines represent the approximate spectrum obtained with 100 time steps. The dotted yellow lines show the spectrum calculated with the monochromatic modulations.

it generated around 600 designs before obtaining a design that has a half-power bandwidth of 50 GHz. The layer thicknesses and doping levels of the optimized design are listed in the last two columns of Table II. The blue-solid and red-dashed curves in Fig. 5 show the spectrum of the original and optimized designs, respectively. The yellow-dotted curve shows the power spectrum of the optimized design, which is obtained with the monochromatic modulation. We observe a difference in the output power, especially for frequencies 40 GHz. However, we achieved our objective of designing a photodetector with a half-power bandwidth that exceeded 50 GHz with a greatly reduced computation time.

The responsivity of the original design is calculated to be 0.47 A/W, corresponding to a quantum efficiency of 0.38. These values for the optimized design are 0.54 A/W and 0.43, respectively. The phase noise of the original and optimized designs are calculated to be −173 and −176 dBc/Hz, respectively, at an operation frequency of 5 GHz. Despite having similar device lengths, 2640 versus 2663 nm, they have different decay times, 37.2 versus 24.8 ps, where the decay time is defined as the difference between the time the electric current reaches its maximum value and the time it takes the electrical current to be reduced to 1% of that maximum value. In Fig. 6, each circle represents the quantum efficiency and bandwidth of one unique design generated during the optimization study, where the fill color changes according to the decay time. In the investigation of photodetectors possessing wide bandwidths (depicted by dark blue circles), it is noted that they exhibit a comparatively lower capacitance when compared to their narrow bandwidth counterparts (represented by yellow circles). This lower capacitance indicates a reduced ability to accumulate charge prior to saturation, facilitating a faster response to variations in light intensity and consequently shorter decay times. Thus, the trend demonstrated in Fig. 6, wherein decay time decreases with increasing bandwidth, is consistent with our expectations.

Since the modulation that is defined with a window function contains a wide range of frequencies with different strengths, the numerical results obtained with this technique will be accurate within machine precisions if the photodetector response to
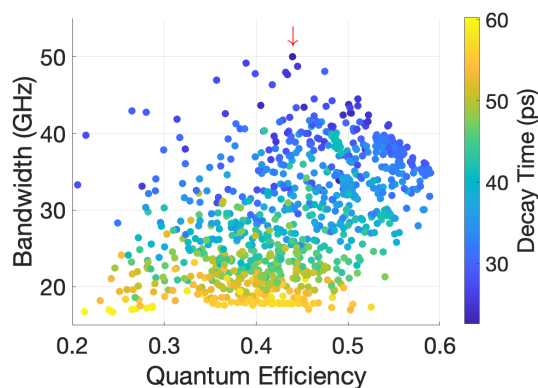
This article has been accepted for inclusion in a future issue of this journal. Content is final as presented, with the exception of pagination.

6   IEEE TRANSACTIONS ON ELECTRON DEVICES

Fig. 6. Quantum efficiency versus bandwidth of more than 600 unique designs generated during the optimization study, where the colors changing from dark blue to yellow represent the decay time. The red down arrow is added to highlight the optimized design's quantum efficiency and bandwidth.

the modulation is linear. The nonlinearities that are induced by space charge are lower at lower powers. So, we anticipate that this approach will work best at low powers, where current compression does not play a significant role. The power threshold up to which this technique is applicable would vary depending on the photodetector structure. The photodetector that we studied has a linear response up to a modulation depth of 0.1.

V. Conclusion

By comparing our numerical results with experiments, we show that the use of window functions enables fast evaluation of the broadband RF output spectrum of photodetectors approximately. This approach makes photodetector design with numerical optimization possible even on desktop computers. We used this approach to optimize the design of a MUTC photodetector. We achieved a speedup of approximately a factor of 200 relative to the computational cost of using a broadband-sinc function modulation, which in turn is faster than monochromatic modulation. Using this approach, we designed a device with a 3-dB bandwidth of 50-GHz, which is four times larger than the bandwidth of our initial design.

References

[1] S. Donati, *Photodetectors: Devices, Circuits and Applications*. Hoboken, NJ, USA: Wiley 2021.

[2] Z. Li, H. Pan, H. Chen, A. Beling, and J. C. Campbell, "High-saturation-current modified uni-traveling-carrier photodiode with cliff layer," *IEEE J. Quantum Electron.*, vol. 46, no. 5, pp. 626–632, May 2010.

[3] Y. Hu, B. S. Marks, C. R. Menyuk, V. J. Urick, and K. J. Williams, "Modeling sources of nonlinearity in a simple p-i-n photodetector," *J. Lightw. Technol.*, vol. 32, no. 20, pp. 3710–3720, Oct. 15, 2014.

[4] S. E. J. Mahabadi et al., "Calculation of the impulse response and phase noise of a high-current photodetector using the drift-diffusion equations," *Opt. Exp.*, vol. 27, vol. 3, pp. 3717–3730, 2019.

[5] D. A. Tulchinsky, J. B. Boos, D. Park, P. G. Goetz, W. S. Rabinovich, and K. J. Williams, "High-current photodetectors as efficient, linear, and high-power RF output stages," *J. Lightw. Technol.*, vol. 26, no. 4, pp. 408–416, Jul. 15, 2008.

[6] E. Rouvalis, A. S. Cross, Q. Zhou, A. G. Steffan, A. Beling, and J. C. Campbell, "A high-power and high-linearity photodetector module with 25 dBm RF output power at 10 GHz," in *Proc. 39th Eur. Conf. Exhib. Opt. Commun.*, 2013, pp. 1–3.

[7] C. Li et al., "High-responsivity vertical-illumination Si/Ge uni-traveling-carrier photodiodes based on silicon-on-insulator substrate," *Sci. Rep.*, vol. 6, no. 1, p. 27743, Jun. 2016.

[8] S. Sun et al., "Zero-bias 32 Gb/s evanescently coupled InGaAs/InP UTC-PDs," *Opt. Laser Technol.*, vol. 101, pp. 457–461, May 2018.

[9] L. Shen et al., "High-bandwidth uni-traveling carrier waveguide photodetector on an InP-membrane-on-silicon platform," *Opt. Exp.*, vol. 24, no. 8, pp. 8290–8301, 2016.

[10] J. Xu, X. Zhang, and A. Kishk, "Design of high speed InGaAs/InP one-sided junction photodiodes with low junction capacitance," *Opt. Commun.*, vol. 437, pp. 321–329, Apr. 2019.

[11] E. Simsek, S. E. J. Mahabadi, I. M. Anjum, and C. R. Menyuk, "Thinner and faster photodetectors producing lower phase noise," in *Proc. IEEE Photon. Conf. (IPC)*, Oct. 2021, pp. 1–14.

[12] E. Simsek, I. M. Anjum, T. F. Carruthers, and C. R. Menyuk, "Designing photodetectors with machine learning," in *Proc. Optica Adv. Photon. Congr.*, 2022, Paper NoW5C.2.

[13] E. Simsek, S. E. J. Mahabadi, I. Md Anjum, and C. R. Menyuk, "A robust drift-diffusion equations solver enabling accurate simulation of photodetectors," in *Proc. Photonics Electromagn. Res. Symp.*, Hangzhou, China, Nov. 2021, p. 1.

[14] E. Simsek et al., "Efficient and accurate calculation of photodetector RF output power," in *Proc. IEEE Photon. Conf. (IPC)*, Vancouver, BC, Canada, Nov. 2022, pp. 1–2.

[15] M. Dentan and B. de Cremoux, "Numerical simulation of the nonlinear response of a p-i-n photodiode under high illumination," *J. Lightw. Technol.*, vol. 8, no. 8, pp. 1137–1144, Jul. 1990.

[16] K. W. Böer, *Survey of Semiconductor Physics*. New York, NY, USA: Van Nostrand, 1990.

[17] W. Fawcett and G. Hill, "Temperature dependence of the velocity/field characteristic of electrons in InP," *Electron. Lett.*, vol. 11, no. 4, pp. 80–81, Feb. 1975.

[18] K. J. Williams, "Microwave nonlinearities in photodiodes," Ph.D. dissertation, Dept. Elect. Eng., Univ. Maryland, College Park, MD, USA, 1994.

[19] M. Razeghi, *Fundamentals of Solid State Engineering*. Cham, Switzerland: Springer, 2006.

[20] Y. Hu, "Modeling nonlinearity and noise in high-current photodetectors," Ph.D. dissertation, Dept. Comput. Sci. Elect. Eng., Univ. Maryland, Baltimore County, MD, USA, 2017.

[21] R. Scaburri, "The incomplete ionization of substitutional dopants in silicon carbide," Ph.D. dissertation, Dept. Mater. Eng., Univ. Bologna, Bologna, Italy, 2011.

[22] G. Xiao, J. Lee, J. J. Liou, and A. Ortiz-Conde, "Incomplete ionization in a semiconductor and its implications to device modeling," *Microelectron. Rel.*, vol. 39, no. 8, pp. 1299–1303, Aug. 1999.

[23] S. Selberherr, *Analysis and Simulation of Semiconductor Devices*. Cham, Switzerland: Springer, 2012.

[24] K. Yang, J. C. Cowles, J. R. East, and G. I. Haddad, "Theoretical and experimental DC characterization of InGaAs-based abrupt emitter HBT's," *IEEE Trans. Electron Devices*, vol. 42, no. 6, pp. 1047–1058, Jun. 1995.

[25] H. Wang and G.-I. Ng, "Avalanche multiplication in InP/InGaAs double heterojunction bipolar transistors with composite collectors," *IEEE Trans. Electron Devices*, vol. 47, no. 6, pp. 1125–1133, Jun. 2000.

[26] F. J. Harris, "On the use of windows for harmonic analysis with the discrete Fourier transform," *Proc. IEEE*, vol. 66, no. 1, pp. 5–83, Jan. 1978.

[27] A. Nuttall, "Some windows with very good sidelobe behavior," *IEEE Trans. Acoust., Speech, Signal Process.*, vol. ASSP-29, no. 1, pp. 84–91, Feb. 1981.

[28] Y. Chen, M.-S. Tong, and R. Mittra, "Efficient and accurate finite-difference time-domain analysis of resonant structures using the Blackman–Harris window function," *Microw. Opt. Technol. Lett.*, vol. 15, no. 6, pp. 389–392, Aug. 1997.

[29] Q.-H. Liu, "Transient electromagnetic modeling with the generalized K-space (GkS) method," *Microw. Opt. Technol. Lett.*, vol. 7, no. 18, pp. 842–848, Dec. 1994.

[30] J. Kennedy and R. Eberhart, "Particle swarm optimization," in *Proc. IEEE Int. Conf. Neural Netw.*, Apr. 1995, pp. 1942–1945.

[31] E. Mezura-Montes and C. A. C. Coello, "Constraint-handling in nature-inspired numerical optimization: Past, present and future," *Swarm Evol. Comput.*, vol. 1, no. 4, pp. 173–194, Dec. 2011.

[32] M. E. Pedersen, *Good Parameters for Particle Swarm Optimization*. Luxembourg, U.K.: Hvass Laboratories, 2010.